Prediction of bead geometry with consideration of interlayer temperature effect for CMT based wire-arc additive manufacturing

WANG Zeya[a]*, ZIMMER-CHEVRET Sandra[b], LEONARD François[a], ABBA Gabriel[a]

a. Université de Lorraine, Arts et Metiers Institute of Technology, LCFC, HESAM Université, F-57070 Metz, France

b. Arts et Metiers Institute of Technology, Université de Lorraine, LCFC, HESAM Université, F-57070 Metz, France

*Corresponding author. E-mail address: zeya.wang@univ-lorraine.fr.

Abstract

Cold metal transfer (CMT) based wire-arc additive manufacturing (WAAM) is increasingly popular for the production of large and complex metallic components due to its high deposition rate, low heat input and excellent material efficiency. The accurate prediction of the bead geometry is of great importance to enhance the stability of the process and its dimensional accuracy. Besides the wire feed speed (WFS) and travel speed (TS), the interlayer temperature is another key factor in determining the bead geometry because of the heat accumulation in the multilayer deposition. In this paper, considering the varying interlayer temperature, WFS and TS as inputs, an artificial neural network (ANN) is developed to predict the bead width, height and contact angle; then, by connecting the ANN model with a bead geometric model, a combined model is established to improve the ANN model. Based on experimental test data, with random combinations of input parameters, the combined model is demonstrated to be able to accurately predict the bead geometry (mean error < 5.1%). The general effect of interlayer temperature on the bead geometry was also investigated by experiment.

Keywords: Accurate prediction, Interlayer temperature, Bead geometry, Process modeling, WAAM

Declarations

Funding: Not applicable.

Conflicts: The authors declare no competing interests.

Availability of data and material: All data generated or analyzed during this study are included in this manuscript.

Code availability: Not applicable.

Acknowledgements

The authors would like to thank the CPER (State-Region contract) Cyber-Enterprises and the Grand Est region funding plans, as well as the technical staff at ENSAM-Arts et Métiers, in particular M. Sylvio De Paolis and M. Daniel Boehm, for their support and investment during the experimental campaign.

1.Introduction

Wire-arc additive manufacturing (WAAM) is a promising technique for fabricating large metallic components through a process of layer-by-layer deposition. It has the advantages of low equipment cost, less material waste, and high production efficiency [1]. Generally, the power source used to melt the metal wire in WAAM can be classified as: gas metal arc welding (GMAW), gas tungsten arc welding (GTAW), and plasma arc welding (PAW), where GMAW is increasingly popular due to its higher deposition rate [2]. Cold metal transfer (CMT) is a modification of GMAW based on a controlled dip transfer mode. It has been widely used for WAAM due to its low heat input and nearly zero spatter [3]. The different arc modes of CMT were investigated to build parts with zero porosity by Cong et al. [4]. Ali et al. [5] analyzed the influence of the arc energy and the thermal field on the resulting mechanical properties and microstructure of the hot work tool steel in CMT based WAAM.

In WAAM, the geometry of the individual weld bead plays a significant role in the determination of the surface quality and dimensional accuracy of the deposited parts. Therefore, there has been much research focused on determining the effects of the process parameters on the single bead geometry. In WAAM of bainite steel, Fu et al. [6] investigated the effect of the interaction of the wire feed speed (WFS) and the travel speed (TS) on the weld bead width (W) and height (H). It was observed that W/H decreases when the WFS is increased for all levels of TS. Ayarkwa et al. [7] found that the key factor is the ratio of the WFS to TS: increasing this ratio increased the bead width and height of aluminium walls manufactured by CMT. Kazanas et al. [8] studied the fabrication of inclined steel and aluminium walls in CMT, with the WFS/TS ratio kept constant. It was found that TS is a major factor for the wall quality, and that a value between 0.2 and 0.25 m/min gives the lowest surface waviness.

In addition to WFS and TS, the interlayer temperature (the temperature of the workpiece at the beginning of the deposition of the subsequent layer or the temperature of the substrate for mono-layer deposition) has also been a frequently discussed parameter [9–11]. Most studies have concentrated on its influence on the microstructural evolution and material properties of the fabricated parts. In the deposition of a simple Ti-Al part of WAAM, it was discovered that a change of the interlayer temperature from 100 °C to 500 °C decreases the fraction of the alpha phase in the microstructure, hence reducing its hardness [12]. It was reported that poorly controlled interlayer temperature is likely to produce longitudinal cracking and high residual stress in the first few layers of Fe-Al components using WAAM process [13]. The interlayer temperature has also been demonstrated to be another critical factor that influences the geometrical accuracy of WAAM. With other parameters kept constant, the bead geometries were reported to vary along the building direction due to increasing interlayer temperatures in WAAM of Ti6Al4V [14]. Xiong et al. [15] investigated the influence of the process parameters on the surface roughness in WAAM and concluded that decreasing the interlayer temperature is associated with an increase of the surface quality of thin-wall parts. During the WAAM process studied in [16], the final forming quality of the steel thin-wall parts improved as the interlayer temperature decreased, within a certain range.

In order to obtain high surface quality and dimensional accuracy in WAAM, all deposited weld beads in each layer have to be predictable and controllable [17]. Thus it is essential to develop process models that enable the prediction of the weld bead geometry from the process parameters. Xiong et al. [18] established models relating GMAW based WAAM process variables (WFS, TS, voltage and nozzle-to-plate distance) and the bead geometry (width and height) using an artificial neural network (ANN) and a second-order regression analysis. Through an analytical model, the layer height and wall width were predicted from the process parameters in pulsed GTAW and PAW WAAM, where the interlayer temperature led to significant geometry variations [19]. In other related fields, ANN was used to associate the process variables with bead geometry in shielded metal-arc welding [20]. A linear regression was applied on the pulsed GMAW modeling for the prediction of the bead geometry [21]. However, little has been reported about taking the interlayer temperature into consideration in the modeling of CMT based WAAM for bead geometry prediction. A model that does not include the effect of the interlayer temperature could be inconvenient for predicting accurately the bead geometry in a multilayer WAAM, where the interlayer temperature varies from layer to layer due to the accumulation of heat. In the deposition of a multilayer ER100 part, it was found that 15 to 26 layers of deposition were needed for the interlayer temperature to stabilize [22]. To avoid the influence of the interlayer temperature, the usual solution is like what Spencer et al. [23] proposed, where, to improve the surface quality, the deposited layer was kept cooled to a certain lower temperature (e.g., 120 °C) before depositing a new layer, but at the expense of reduced efficiency (cooling time accounted for more than twice the actual build time). This effect on the efficiency could become worse when producing large parts because of the much longer cooling time.

In the present paper, with the consideration of the interlayer temperature and other process parameters (WFS and TS), the prediction of the bead geometry has been realized through an ANN model and then a further combined model, based on connecting the ANN and a weld bead geometric model. The contact angle was introduced to develop the weld bead geometric model: it is a crucial factor in CMT welding, determining directly the geometry of the bead [24]. The geometric model enables the improvement of the prediction accuracy of the width and height of the bead. At different interlayer temperatures, the established combined model allows predicting the geometry of the weld bead with precision, which consequently contributes to enhance the controllability and efficiency of the process. It should be noticed that the establishment of the proposed model is based on single layer deposition experiments, while it can allow the prediction of bead geometry for the fabrication of multilayer pieces with the interlayer temperature considered as one of the model inputs.

2. Methodology

2.1 Experimental set-up

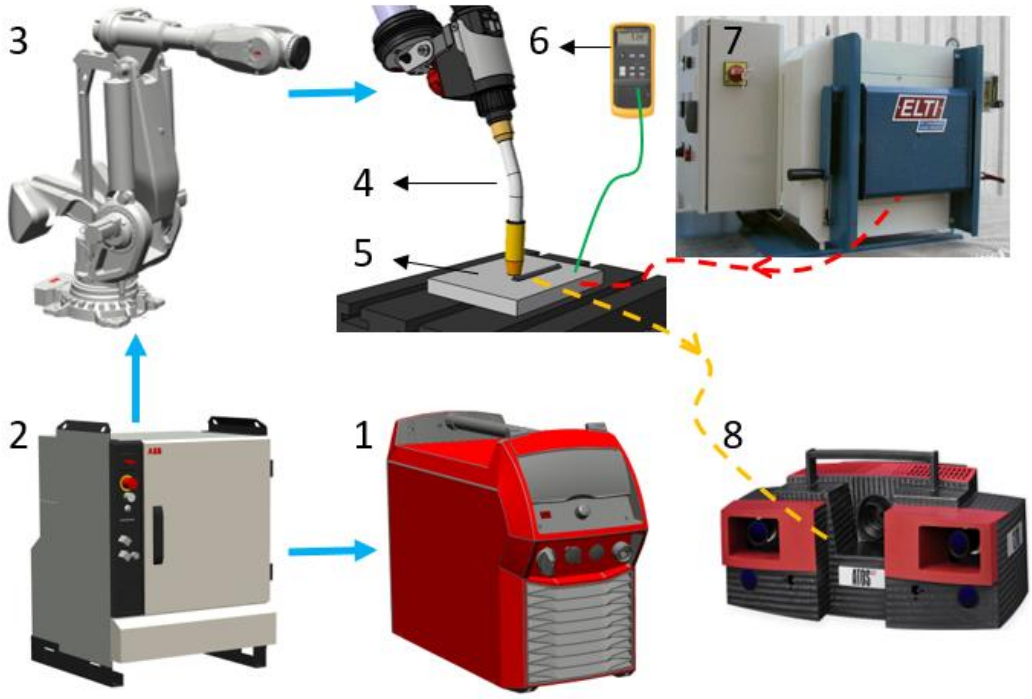

Fig. 1 Schematic diagram of the experimental set-up (1. welding source, 2. control cabinet, 3. robot, 4. torch, 5. substrate, 6. thermocouple, 7. furnace, 8. 3D scanner)

A schematic diagram of the experimental set-up is shown in Fig. 1. A CMT welding power source (Fronius TPS320i) and an ABB IRB8700 robot were connected through the robot control cabinet, which was used to coordinate both the motions of the robot and the CMT process. With the torch mounted, the robot was employed to execute the deposition path. The material of the consumable wire electrode was copper coated ER100 high strength steel with a diameter of 1.2 mm. The chemical composition of the wire (in wt. %) is provided in Table 1. A gas mixture of Ar (85 %) and CO2 (15 %) with a flow rate of 18 l/min was used for shielding. Single weld beads were deposited on the substrate, which was made of mild steel S235 which was 200 mm long, 150 mm wide, and a height of 20 mm. Before the deposition, the substrate was sandblasted to remove the oxides and to maintain a good and consistent surface quality. An electric furnace (ELTI Easylab 304) was used to heat the substrate in order to achieve higher interlayer temperatures for experimental single beads (for single beads, the interlayer temperature is the substrate surface temperature). The substrate was removed from the furnace before the beginning of the deposition and its surface temperature was checked with a contact thermocouple at the starting point of the bead deposition, to ensure that the experimental set value was reached. During the deposition process, the torch was held perpendicular to the substrate, and the nozzle-to-plate distance was kept at 15 mm. The deposited beads were sandblasted again for the measurement by an optical 3D scanner (ATOS Triple Scan), which was employed to measure quickly and accurately the deposited beads' geometry. As illustrated in the Fig. 2, the length of the beads was set at 100 mm, and the middle 50 mm section was taken as the area for the acquisition of the measured data; it is where the bead geometry is stable, whereas the beginning and the end of the weld bead correspond to the arc ignition

and extinguishment phases, which degrade the consistency of the bead geometry. The mean value of the data acquired is used as the final measurement result.

Table 1

Composition of the wire material ER100

Element	C	Si	Mn	Cr	Ni	Mo	P	S	V	Ti	Zr	Al	Cu	Fe
Wt.%	0.08	0.54	1.66	0.25	1.58	0.47	0.007	0.01	0.002	0.05	0.001	0.002	0.14	Bal.

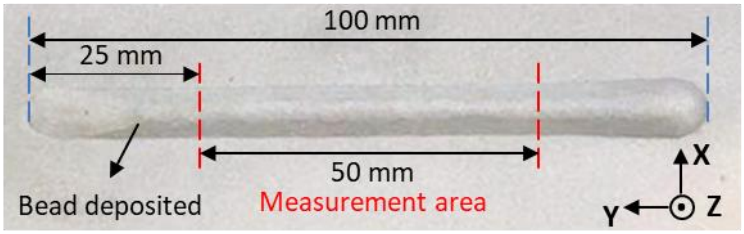

Fig. 2 Illustration of the bead deposited and sandblasted for the measurement by 3D scanner

2.2 Input and output selection

In a CMT welding source, based on the given data (wire material and diameter, welding mode, type of shielding gas), the welding voltage and current parameters are automatically adjusted according to the user input WFS to obtain stable and continuous metal transfer. Therefore, three independent process parameters, WFS, TS and the interlayer temperature (T_{int}), have been considered as the input. The width *W*, height *H* and contact angle θ_c (the geometric characteristics of the weld bead) were selected for the output. They are illustrated in Fig. 3.

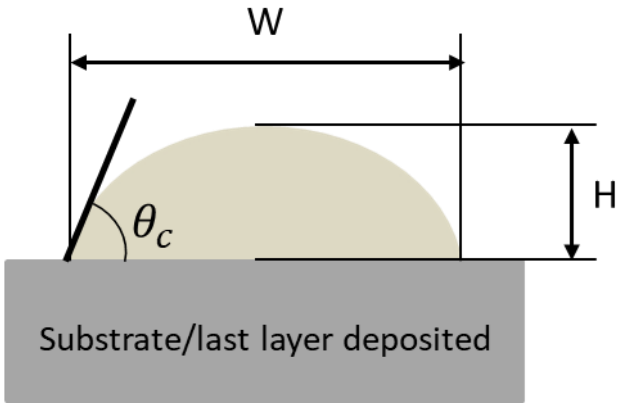

Fig. 3 Illustration of single bead geometry

The contact angle at the solid-liquid-gas interface is the angle that the liquid weld bead interacts with the substrate (or previous layer); thus, when the deposition rate is constant, a variation in the contact angle directly affects the final geometry of the bead after solidification. Furthermore, in CMT multi-bead deposition, the quality of the overlap also depends on the single bead's contact angle [25]. Consequently, the prediction of the contact angle helps significantly in selecting a suitable bead for the WAAM process, which is why it was included in the output. The limits for the process input parameters were determined by a

set of preliminary experiments, which ensure that the bead geometry has no defects. Table 2 gives the limits for the values of the process parameters, identifying various divisions of their levels for the later experiments.

Table 2

Process parameters limit values at various levels

	Level 1	Level 2	Level 3	Level 4	Level 5
WFS (m/min)	5.0	6.0	7.5	9.0	10.0
TS (mm/s)	6.0	7.6	10.0	12.4	14.0
T_{int} (°C)	50.0	160.0	325.0	490.0	600.0

2.3 Artificial neural network modeling

In the CMT welding process, many physical mechanisms, especially thermal ones, are involved and act directly on the morphology of the bead [26], which leads to complex relations between the process parameters and the geometry of the weld bead. Artificial neural networks (ANN) have been proven to be an efficient method for dealing with complex relations between multiple inputs and outputs: it is able to predict the outcome based on preset input parameters and to optimize manufacturing processes, especially for the strong nonlinearity in the welding process [27]. In order to predict the bead geometry in our case, a multilayer neural network with one hidden layer was applied, where a back-propagation algorithm was used to train the network. This structure is the simplest and most commonly used: it enables the network to simulate nonlinearity in practical systems. Fig. 4 presents its schematic diagram. The neurons in the different layers are the basic computational units, based on the nonlinear sigmoid transfer function. They are responsible for a nonlinear mapping between the inputs (WFS, TS, T_{int}) and outputs (W, H, θ_c). Generally, with the training data provided from experiments, the network outputs are compared with the desired outputs. Then the connection weights inside the network are adjusted, based on the back-propagation learning algorithm, to minimize the differences. The training process is iterative and will stop once an acceptable error is achieved.

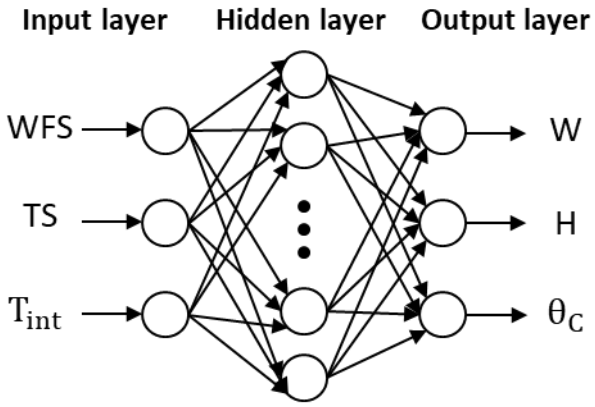

Fig. 4 Schematic diagram of the multilayer neural network

To guarantee the integrity and sufficiency of the experimental data collected for the network training, the data collection experiments were designed based on a three-factor central composite design. The values of the parameters of the process were

divided into five levels (as shown in Table 2). Thus, 30 experiments were carried out for the network training. Table 3 shows the different combinations of parameters and their responses, where experiments 1-15 came from the experimental design, and 16-30 were added as extras to enrich the training data. The collected data was linearly normalized to lie within the interval [0, 1] before training, to guarantee that each input parameter had the same contribution to the training, which leads to a better performance of the network.

Table 3

Experimental data for the network training

No.	Input			Output		
	WFS (m/min)	TS (mm/s)	T_{int} (°C)	W (mm)	H (mm)	θ_C (°)
1	6.00	7.60	160.00	8.25	3.01	50.95
2	6.00	7.60	490.00	8.75	2.45	44.56
3	6.00	12.40	160.00	6.83	2.42	52.19
4	6.00	12.40	490.00	7.14	1.90	45.10
5	9.00	7.60	160.00	9.17	3.88	53.05
6	9.00	7.60	490.00	9.20	3.46	52.49
7	9.00	12.40	160.00	7.86	3.15	54.55
8	9.00	12.40	490.00	7.23	2.99	54.15
9	5.00	10.00	325.00	8.14	1.90	39.42
10	10.00	10.00	325.00	9.72	3.38	50.13
11	7.50	6.00	325.00	11.82	3.37	40.19
12	7.50	14.00	325.00	7.97	2.15	41.06
13	7.50	10.00	50.00	9.42	3.06	46.23
14	7.50	10.00	600.00	7.52	3.20	55.49
15	7.50	10.00	325.00	9.60	2.64	40.99
16	7.50	8.00	100.00	9.24	3.41	50.00
17	6.10	9.00	300.00	7.32	3.01	53.27
18	6.30	7.00	500.00	8.36	3.31	52.50
19	7.40	14.00	50.00	7.56	2.32	48.18
20	6.50	14.00	600.00	6.53	2.38	55.61
21	7.20	6.00	325.00	11.45	3.35	42.01
22	7.20	10.00	325.00	9.49	2.48	39.26
23	5.30	10.00	325.00	8.21	2.02	41.96
24	7.40	10.00	325.00	9.58	2.59	41.52
25	7.10	10.00	325.00	9.27	2.42	40.10
26	7.00	14.00	325.00	7.96	2.08	41.14
27	6.30	12.00	500.00	7.12	2.43	52.98
28	6.10	14.00	300.00	6.20	2.39	56.44
29	7.10	10.00	325.00	9.19	2.48	40.23
30	7.40	10.00	325.00	9.55	2.61	41.49

The number of the neurons at the hidden layer is a key factor in determining the result of neural network training. As there is no general rule for the selection of the number, it's usually decided by trial and error to achieve minimum prediction errors.

During the network training, the prediction errors were calculated by the mean square error (MSE) defined in Eq. (1) as the performance function of the training:

$$MSE = \frac{1}{2MN}\sum_{i=1}^{M}\sum_{k=1}^{N}\left(y_r^{ik} - y_p^{ik}\right)^2 \quad (1)$$

Here, *M* represents the amount of training data, *N* is the number of the outputs, while y_r^{ik}, respectively, y_p^{ik}, are the real and predicted output values. Different numbers of hidden-layer neurons were tested to train the network. Finally, the number 14 was adopted, where the minimum MSE of 3.232×10^{-5} was obtained. Table 4 presents the ANN training results in the form of the prediction errors (%) for each output. Besides the training, it is also necessary to test the network by data that are unknown to the trained network, to evaluate its effectiveness. This will be discussed in section 3.1.

Table 4

ANN training results represented by the prediction errors (%)

Output		W	H	θ_C
Error (%)	Maximum	2.64	2.68	1.07
	Mean	0.91	0.84	0.61

2.4 Combined model developed from the geometric model of the bead

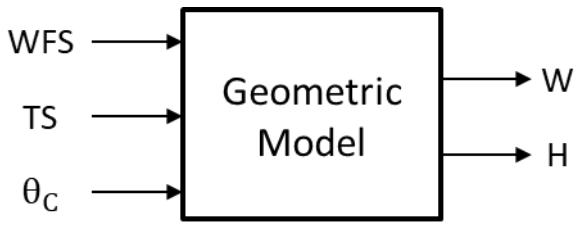

Fig. 5 Schematic diagram of the geometric model of a single bead

Fig. 5 shows a schematic diagram of the single bead geometric model, which relates the process parameters WFS, TS and contact angle to the width and height of the weld bead. The model could help mathematically explain how the process parameters affect the final geometry of the weld bead. In wire arc welding, the ratio WFS/TS (WFS and TS are expressed in the same units) determines the amount of material deposited per unit length, also known as the area of the cross-section of a single weld bead, defined in Eq. (2):

$$S = \pi\frac{{d_w}^2}{4} \times \frac{WFS}{TS} \quad (2)$$

Here, *S* is the cross-sectional area of the bead and d_w is the diameter of the metal wire. Then the cross-sectional profile of the bead was modeled by the circular arc as illustrated in Fig. 6.

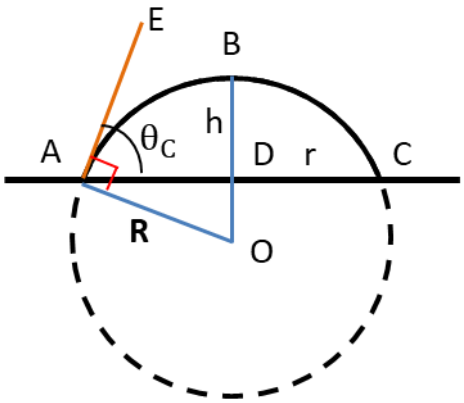

Fig. 6 Modeling the cross-sectional profile of the bead

In the figure, the circular arc $\overset{\frown}{AC}$ (drawn with a solid line) represents the profile of the bead. The horizontal line AC represents the substrate or previous layer surface, OA = OB = R is the radius of the arc, the radius OB and the chord AC intersect vertically at the point D (BD=h, AD=CD=r), since AE is tangent to the arc (by the definition of contact angle θ_c), AE is perpendicular to OA. Consequently, $\angle AOB = \theta_C$, and the area of the part ABC (namely, the bead's cross-sectional area *S*) can be expressed by

$$S = \theta_c R^2 - r(R - h) \tag{3}$$

Also, the relations between *r*, *h*, θ_c and *R* can be expressed by

$$R = \frac{r}{\sin\theta_C} \tag{4}$$

$$h = (1 - \cos\theta_C)\frac{r}{\sin\theta_C} = r\tan\frac{\theta_C}{2} \tag{5}$$

Combining Eqs. (2), (3), (4) and (5), the width and height of the bead can be obtained:

$$W = 2r = 2\sqrt{\frac{\pi\frac{{d_w}^2}{4}\times\frac{WFS}{TS}}{\left(\frac{\theta_C}{\sin^2\theta_C} - \frac{1}{\sin\theta_C} + \tan\frac{\theta_C}{2}\right)}} \tag{6}$$

$$H = h = r\tan\frac{\theta_C}{2} = \sqrt{\frac{\pi\frac{{d_w}^2}{4}\times\frac{WFS}{TS}}{\left(\frac{\theta_C}{\sin^2\theta_C} - \frac{1}{\sin\theta_C} + \tan\frac{\theta_C}{2}\right)}}\tan\frac{\theta_C}{2} \tag{7}$$

In Eqs. (6) and (7), the developed geometric model also demonstrates the important role of the contact angle in the determination of the width and height of the deposited weld bead, thus also indirectly including the effects of the different interlayer temperatures on the geometry of the bead. However, the contact angle is not an input parameter that can be directly controlled (it is the result of complex thermal mechanisms in the process). This problem was solved by connecting the geometric model to the trained ANN model through θ_c. Thus a combined model was obtained which is also able to output the geometry of the bead (θ_c as predicted by ANN, as well as *W* and *H* as calculated by the geometric model) from the input WFS, TS, and the

interlayer temperature. Fig. 7 presents a schematic diagram of this combined model, where the contact angle output by the ANN was taken as one of the inputs of the geometric model.

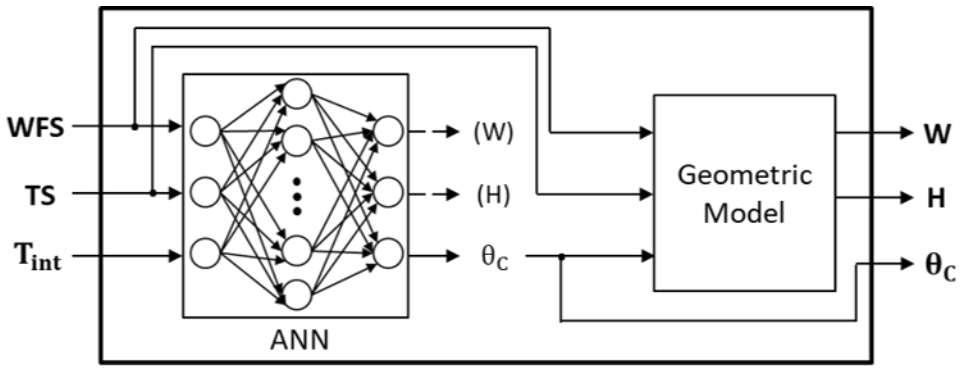

Fig. 7 Schematic diagram of the combined model consisting of the ANN and the geometric model

3. Results and discussion

Additional experiments were performed to test the accuracy of the established models (the ANN model, the geometric model, and the combined model) for predicting the geometry of weld beads deposited by the CMT based WAAM process.

3.1 Performance of the trained ANN model

Table 5

Experimental data for the tests

No.	Input			Output		
	WFS (m/min)	TS (mm/s)	T_{int} (°C)	W (mm)	H (mm)	θ_C (°)
1	5.70	10.00	500.00	7.97	2.14	43.34
2	6.90	10.00	500.00	8.09	2.82	48.83
3	9.10	10.00	500.00	8.55	3.36	48.40
4	5.10	10.00	250.00	6.99	2.25	49.12
5	5.90	10.00	250.00	7.23	2.54	50.52
6	7.20	10.00	250.00	7.38	3.11	55.86
7	9.10	10.00	250.00	7.79	3.47	65.10
8	5.80	7.60	250.00	7.95	2.92	51.99
9	5.90	12.40	250.00	6.98	2.25	49.37
10	9.00	7.60	250.00	9.37	4.04	56.85
11	9.30	12.40	250.00	7.61	3.66	59.74
12	8.22	10.00	50.00	9.42	3.06	46.23
13	5.78	8.00	600.00	7.52	3.20	55.49
14	6.56	7.00	100.00	9.24	3.41	50.00
15	5.42	8.00	300.00	7.32	3.01	53.27
16	7.20	8.00	500.00	8.36	3.31	52.50
17	6.87	13.00	50.00	7.56	2.32	48.18
18	5.57	12.00	600.00	6.53	2.38	55.61
19	7.35	14.00	500.00	7.12	2.43	52.98
20	5.66	13.00	300.00	6.20	2.39	56.44
21	6.92	12.00	100.00	7.75	2.62	48.69

In order to evaluate the effectiveness of the trained ANN, extra experimental data need to be used to test the network in real conditions, and these data should be unknown to the network (different from the data used for training). Therefore, 21 experiments were carried out with varied values of the input parameters (WFS, TS, T_{int}) within their defined limits, where the combinations of these input parameters were different from any of the ones shown in Table 3. Table 5 presents the input and output data of these experimental data for the tests. As in the training work, the test data was linearly normalized within [0, 1] for the application of the ANN.

The test results of the ANN model are presented in Fig. 8 and Table 6 (a). It can be seen that the developed model predicted well the value of the contact angle (mean error 2.97% and maximum error 4.75%), but the prediction errors were bigger for the width and height (mean error > 6% and maximum error > 10%). Since the interlayer temperature was introduced as the input

parameter of the process, with the variation of all three input parameters, the geometry of the weld beads fluctuated more, hence the input-output relationship of the process was more complex compared to the case of a constant interlayer temperature, which made the prediction more difficult with a single ANN model.

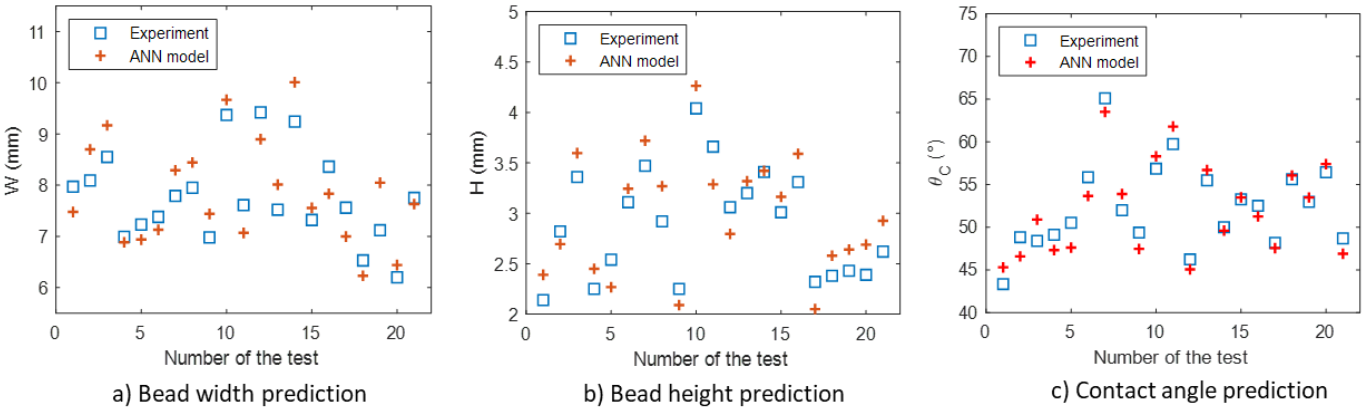

Fig. 8 Results of the ANN model compared with the experimental measurements

Table 6

Test results represented by the prediction errors (%)

Output		W	H	θ_C
Error (%)	Maximum	11.01	10.89	4.75
	Mean	6.70	7.83	2.97

a) Test results of the ANN model

Output		W	H	θ_C
Error (%)	Maximum	7.29	8.54	4.75
	Mean	3.63	5.05	2.97

b) Test results of the combined model

3.2 Test of the geometric model with different interlayer temperatures

For the purpose of testing the performance of the established geometric model at predicting the width and height of the bead in the presence of different interlayer temperatures, and also to identify the effect of the interlayer temperature on the geometry of the bead, two groups of experiments were performed. Each group contained seven different interlayer temperatures, varying from 50°C to 600°C with WFS and TS held constant, and each group of experiments was repeated three times. The WFS was set at 7.5 m/min for the two groups. The TS in the first group was 13 mm/s and 8 mm/s in the second one. Then the WFS, TS and the measured θ_c were employed as the input to the model, the geometric model outputs W and H were compared with the real values. Fig. 9 shows this comparison. For all 56 experiments conducted in the two groups, the maximum and mean prediction errors by the model were 3.85% and 2.16% for W, and 7.49% and 3.34% for H. These test results imply that the geometric model is able to predict the width and height of the bead more accurately than the ANN model developed in our case when considering the effect of the interlayer temperature, which can be helpful to improve the prediction of the width and height in the proposed

combined model. The effect of the interlayer temperature will be discussed in section 3.4. It should be noticed that when applying the geometric model to the combined model, one of its inputs the contact angle comes from the prediction of the ANN model, thus the sensitivity of the geometric model to errors in the contact angle is analyzed and discussed in section 3.3.

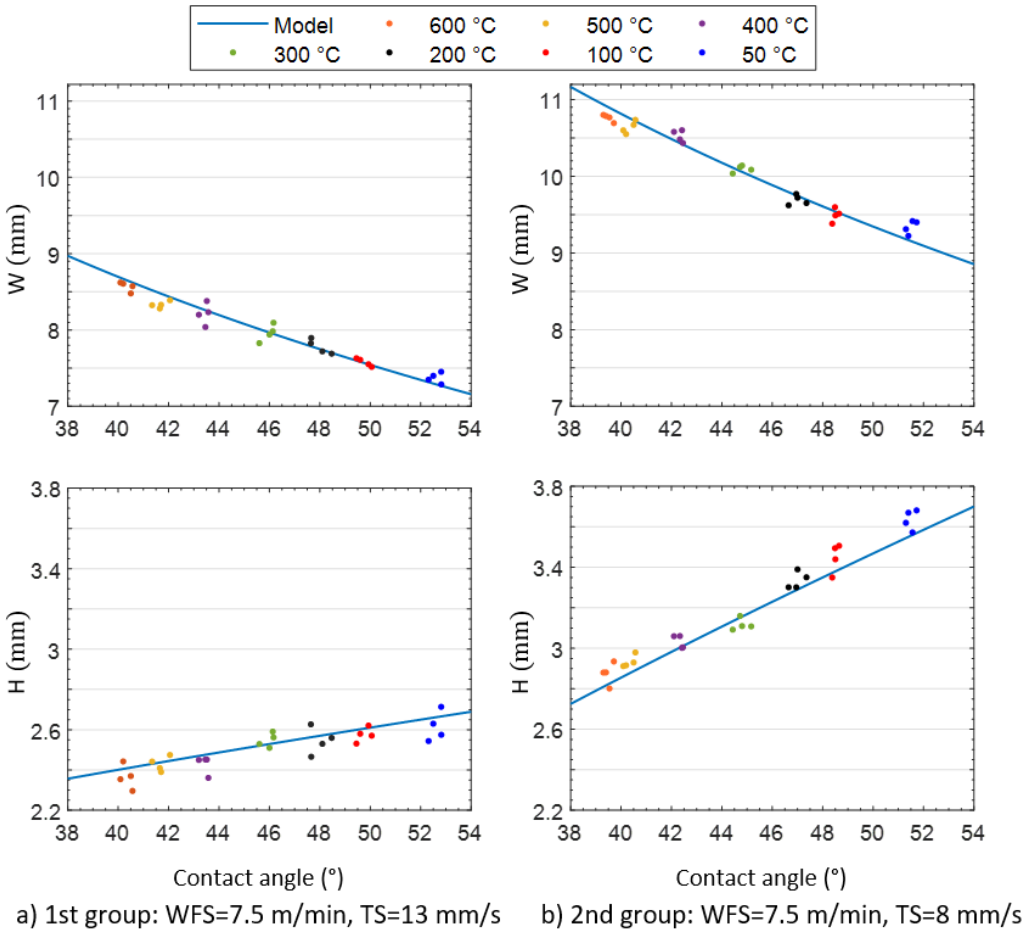

Fig. 9 Comparison between geometric model output (W, H) and experimental values in different interlayer temperatures

3.3 Performance of the combined model

The ANN model and geometric model were combined to form the combined model: the ANN is responsible for providing the prediction of the contact angle and the geometric model is responsible for determining the width and height of the bead, based on the WFS, TS and the predicted contact angle. The experimental data shown in Table 5 for the tests of the ANN were also used to test the combined model. Fig. 10 presents a comparison of the experimental measurements of the geometry of the weld bead (W, H and θ_c) with the predictions of the combined model. Table 6 (b) gives the prediction errors of the combined model. It can be seen that the combined model can give a good prediction of the geometry of the bead. For each of the three outputs, the mean error is less than 5.1%, and the maximum error is less than 8.6%. Compared with the ANN model (corresponding test results shown in Fig. 8 and Table 6 (a)), the combined model was found to improve the prediction accuracy for the width and height. When the same ANN model was connected to the geometric model, the resulting combined model realizes better predictions for the width and height without requiring a heavy experimental campaign to train the neural network:

the mean prediction errors for the width, respectively, the height, decreased from 6.70% and 7.83% to 3.63% and 5.05%. The maximum prediction errors for the width and height were also reduced: from 11.01% and 10.89% for the ANN to 7.29% and 8.54% for the combined model.

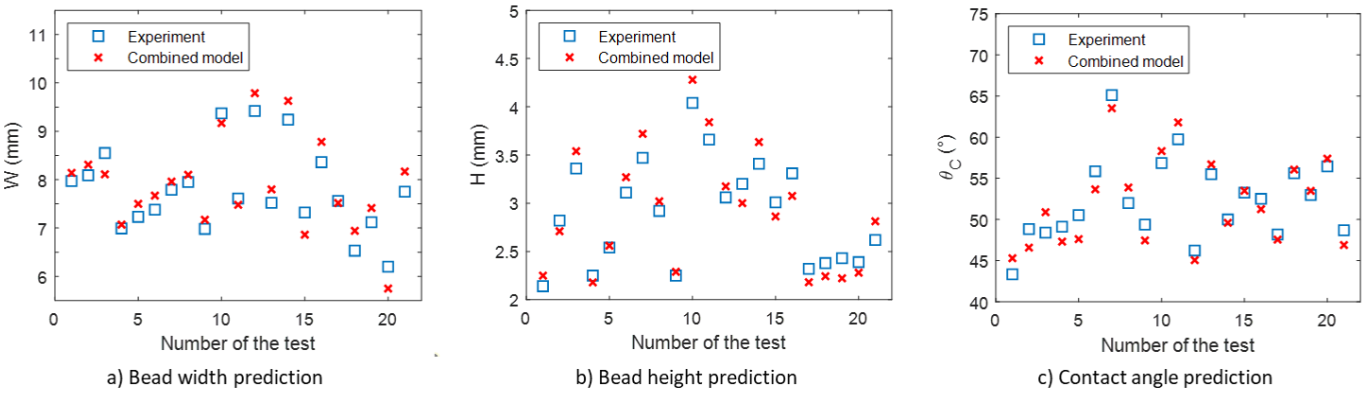

Fig. 10 Results of the combined model compared with the experimental measurements

In the combined model, the contact angle is an input to the geometric model and it comes from the ANN's prediction. There is, then, an inevitable effect of any error in this parameter on the combined model's accuracy in predicting the width and height. Thus the sensitivity of the geometric model to variations in the contact angle was analyzed by calculating the derivative of the width and height with respect to the contact angle (mm/°). Based on Eqs. (6) and (7), $dW/d\theta_c$ and $dH/d\theta_c$ were calculated when the WFS/TS was kept at the maximum ratio (WFS=10 m/min, TS= 6mm/s) where the width and height are most sensitive to any variation of the contact angle. The results are shown in Fig. 11: the range of variation of the contact angle was set at 40° to 60°, which is the most frequent interval. The mean values of $dW/d\theta_c$ and $dH/d\theta_c$ within this interval were -0.17 mm/° and 0.034 mm/° while the corresponding mean width and height calculated by the model were 12.40 mm and 4.14 mm. For example, for a weld bead with a real contact angle of 50°, in the most sensitive case (maximum WFS/TS ratio reached), a mean ANN model prediction error of 2.97% would lead to a width and height errors of 0.25 mm and 0.04 mm, respectively. This analysis shows that the ANN's contact angle prediction error has limited effect on the combined model's width and height prediction accuracy, which can also explain the ability of the combined model to improve the width and height prediction accuracy.

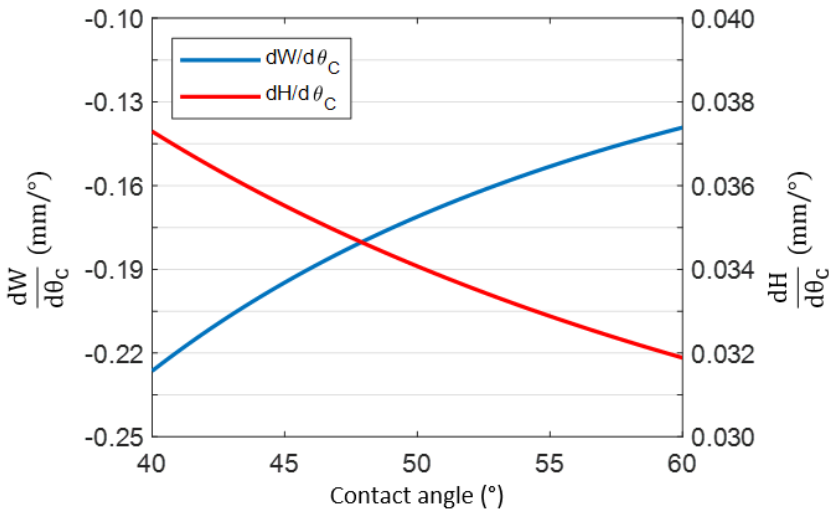

Fig. 11 The derivative of the width and height with respect to the contact angle when WFS=10 m/min, TS=6 mm/s

3.4 Effect of the interlayer temperature

During the experiments testing the geometric model, as single beads were deposited with interlayer temperatures of 50°C, 100°C, 200°C, 300°C, 400°C, 500°C, and 600°C while maintaining the WFS and TS were fixed, the general effect of the interlayer temperature can be inferred by the resulting bead geometry shown in Fig. 9 in scattered points. For both groups of experiments, an increase in the interlayer temperature led to a decrease in the contact angle (mean value from 52.5° to 40.5° for the first group, and from 51.6° to 39.4° for the second). The change in contact angle was most sensitive to the interlayer temperature when the temperature range was 50°C-100°C or 300°C-400°C (a maximum variation of around 3° for each). In contrast, when the interlayer temperature was high enough (in the interval 500°C-600°C), it had the weakest effect on the contact angle, about 1°/100°C. Consequently, the interlayer temperature also affects the width and height of the bead by affecting the contact angle. An increase in interlayer temperature resulted in a larger width and at the same time a reduced height due to the fixed cross-sectional area via the constancy of the ratio WFS/TS. The width and height in the second group were larger than in the first group, and their ranges of variation were also greater, due to there being more material deposited per unit length (smaller TS). In order to show the general effect of the interlayer temperature on the geometry of a single bead, Fig. 12 presents an example of the measurement results provided by the 3D optical scanner for the cross-sectional profiles in the middle of beads deposited in the first group (one for each different interlayer temperature).

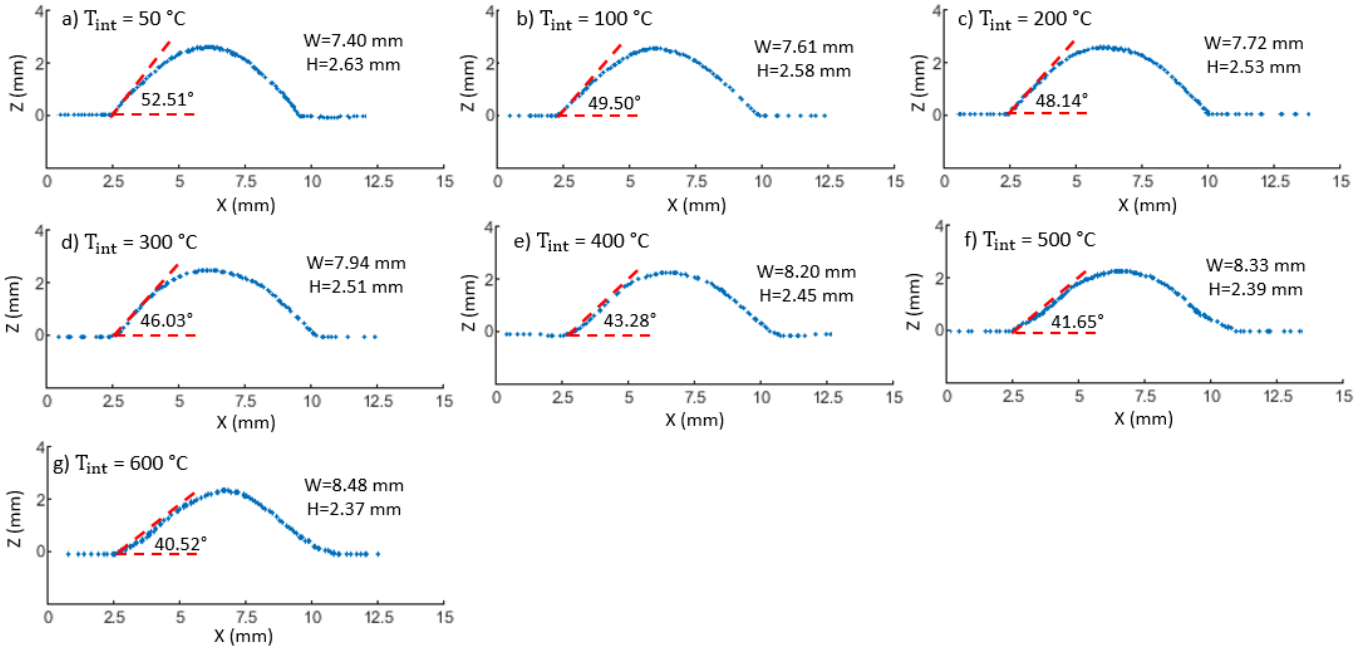

Fig. 12 Measurement results of the cross-sectional profiles in the middle of beads deposited with WFS=7.5 m/min, TS=13 mm/s and different interlayer temperatures

4. Conclusions

This paper investigates the prediction of single weld bead geometry for cold metal transfer (CMT) based wire-arc additive manufacturing (WAAM) with the aim of improving the stability and efficiency of the process. In addition to the wire feed speed (WFS) and travel speed (TS), the effect of the interlayer temperature was also considered during the modeling of the process. An artificial neural network (ANN) model and a combined model (ANN + a geometric model) were developed and shown to be able to effectively predict the width, height and the contact angle of weld beads. The following conclusions can be drawn:

An ANN model has been developed for the data mapping between the process inputs (WFS, TS and interlayer temperature) and the geometry of the bead. According to the test results, the ANN model could predict well the contact angle with a mean prediction error less than 3%, but its predictions of the width and height were very satisfactory (the mean errors are greater than 6.70%).

A geometric model of a single weld bead was developed to relate the WFS, TS, and contact angle to the width and height of the weld bead, which mathematically demonstrated the significant influence of the WFS/TS ratio and contact angle on the geometry of the bead. The accuracy of this model was verified by experiments (mean prediction errors < 3.4% for both width and height).

The ANN model was then connected with the geometric model to generate a combined model, where the contact angle predicted by the ANN was used as one input of the geometric model. Compared to the ANN model, the combined model improved the prediction accuracy (mean errors 3.63% for the width and 5.05% for the height) without requiring a heavy experimental campaign to train the neural network.

The general effect of the interlayer temperature on the geometry of the bead was analyzed. With the other parameters being constant, an increase of the interlayer temperature decreased the contact angle of the weld bead, resulting in the bead becoming smaller in height but wider.

References

1. Ding D, Pan Z, Cuiuri D, Li H (2015) Wire-feed additive manufacturing of metal components: technologies, developments and future interests. Int J Adv Manuf Technol 81:465–481. https://doi.org/10.1007/s00170-015-7077-3

2. Le VT, Paris H (2021) On the use of gas-metal-arc-welding additive manufacturing for repurposing of low-carbon steel components: microstructures and mechanical properties. Weld World. https://doi.org/10.1007/s40194-020-01005-y

3. Frostevarg J, Kaplan AFH, Lamas J (2014) Comparison of CMT with other arc modes for laser-arc hybrid welding of steel. Weld World. https://doi.org/10.1007/s40194-014-0146-7

4. Cong B, Ding J, Williams S (2015) Effect of arc mode in cold metal transfer process on porosity of additively manufactured Al-6.3%Cu alloy. Int J Adv Manuf Technol 76:1593–1606. https://doi.org/10.1007/s00170-014-6346-x

5. Ali Y, Henckell P, Hildebrand J, et al (2019) Wire arc additive manufacturing of hot work tool steel with CMT process. J Mater Process Technol 269:. https://doi.org/10.1016/j.jmatprotec.2019.01.034

6. Fu Y, Wang G, Zhang H, Liang L (2017) Optimization of surface appearance for wire and arc additive manufacturing of Bainite steel. Int J Adv Manuf Technol. https://doi.org/10.1007/s00170-016-9621-1

7. Ayarkwa KF, Williams S, Ding J (2015) Investigation of pulse advance cold metal transfer on aluminium wire arc additive manufacturing. Int J Rapid Manuf 5:44. https://doi.org/10.1504/ijrapidm.2015.073547

8. Kazanas P, Deherkar P, Almeida P, et al (2012) Fabrication of geometrical features using wire and arc additive manufacture. Proc Inst Mech Eng Part B J Eng Manuf. https://doi.org/10.1177/0954405412437126

9. Zhao W, Wei Y, Long J, et al (2021) Modeling and simulation of heat transfer, fluid flow and geometry morphology in GMAW-based wire arc additive manufacturing. Weld World. https://doi.org/10.1007/s40194-021-01123-1

10. Vázquez L, Rodríguez N, Rodríguez I, et al (2020) Influence of interpass cooling conditions on microstructure and tensile properties of Ti-6Al-4V parts manufactured by WAAM. Weld World. https://doi.org/10.1007/s40194-020-00921-3

11. Reisgen U, Sharma R, Mann S, Oster L (2020) Increasing the manufacturing efficiency of WAAM by advanced cooling strategies. Weld World. https://doi.org/10.1007/s40194-020-00930-2

12. Ma Y, Cuiuri D, Shen C, et al (2015) Effect of interpass temperature on in-situ alloying and additive manufacturing of titanium aluminides using gas tungsten arc welding. Addit Manuf 8:71–77. https://doi.org/10.1016/j.addma.2015.08.001

13. Shen C, Pan Z, Cuiuri D, et al (2017) Influences of deposition current and interpass temperature to the Fe3Al-based iron aluminide fabricated using wire-arc additive manufacturing process. Int J Adv Manuf Technol 88:2009–2018. https://doi.org/10.1007/s00170-016-8935-3

14. Wu B, Ding D, Pan Z, et al (2017) Effects of heat accumulation on the arc characteristics and metal transfer behavior in Wire Arc Additive Manufacturing of Ti6Al4V. J Mater Process Technol 250:304–312. https://doi.org/10.1016/j.jmatprotec.2017.07.037

15. Xiong J, Li Y, Li R, Yin Z (2018) Influences of process parameters on surface roughness of multi-layer single-pass thin-walled parts in GMAW-based additive manufacturing. J Mater Process Technol 252:128–136. https://doi.org/10.1016/j.jmatprotec.2017.09.020

16. Yang D, Wang G, Zhang G (2017) Thermal analysis for single-pass multi-layer GMAW based additive manufacturing using infrared thermography. J Mater Process Technol 244:215–224. https://doi.org/10.1016/j.jmatprotec.2017.01.024

17. Xiong J, Zhang G, Hu J, Li Y (2013) Forecasting process parameters for GMAW-based rapid manufacturing using closed-loop iteration based on neural network. Int J Adv Manuf Technol 69:743–751. https://doi.org/10.1007/s00170-013-5038-2

18. Xiong J, Zhang G, Hu J, Wu L (2014) Bead geometry prediction for robotic GMAW-based rapid manufacturing through a neural network and a second-order regression analysis. J Intell Manuf 25:157–163. https://doi.org/10.1007/s10845-012-0682-1

19. Ríos S, Colegrove PA, Martina F, Williams SW (2018) Analytical process model for wire + arc additive manufacturing. Addit Manuf 21:. https://doi.org/10.1016/j.addma.2018.04.003

20. Nagesh DS, Datta GL (2002) Prediction of weld bead geometry and penetration in shielded metal-arc welding using artificial neural networks. J Mater Process Technol 123:303–312. https://doi.org/10.1016/S0924-0136(02)00101-2

21. Rao PS, Gupta OP, Murty SSN, Rao ABK (2009) Effect of process parameters and mathematical model for the prediction

of bead geometry in pulsed GMA welding. Int J Adv Manuf Technol. https://doi.org/10.1007/s00170-009-1991-1

22. Bourlet C, Zimmer-Chevret S, Pesci R, et al (2020) Microstructure and mechanical properties of high strength steel deposits obtained by Wire-Arc Additive Manufacturing. J Mater Process Technol. https://doi.org/10.1016/j.jmatprotec.2020.116759

23. Spencer JD, Dickens PM, Wykes CM (1998) Rapid prototyping of metal parts by three-dimensional welding. Proc Inst Mech Eng Part B J Eng Manuf 212:175–182. https://doi.org/10.1243/0954405981515590

24. Hu S, Zhang H, Wang Z, et al (2016) The arc characteristics of cold metal transfer welding with AZ31 magnesium alloy wire. J Manuf Process. https://doi.org/10.1016/j.jmapro.2016.10.001

25. Ola OT, Doern FE (2014) A study of cold metal transfer clads in nickel-base INCONEL 718 superalloy. Mater Des. https://doi.org/10.1016/j.matdes.2013.12.060

26. Selvi S, Vishvaksenan A, Rajasekar E (2018) Cold metal transfer (CMT) technology - An overview. Def Technol 14:28–44. https://doi.org/10.1016/j.dt.2017.08.002

27. Manikya Kanti K, Srinivasa Rao P (2008) Prediction of bead geometry in pulsed GMA welding using back propagation neural network. J Mater Process Technol. https://doi.org/10.1016/j.jmatprotec.2007.09.034

Figure Captions

Fig. 1. Schematic diagram of the experimental set-up (1. welding source, 2. control cabinet, 3. robot, 4. torch, 5. substrate, 6. thermocouple, 7. furnace, 8. 3D scanner)

Fig. 2. Illustration of the bead deposited and sandblasted for the measurement by 3D scanner

Fig. 3. Illustration of single bead geometry

Fig. 4. Schematic diagram of the multilayer neural network

Fig. 5. Schematic diagram of the geometric model of a single bead

Fig. 6. Modeling the cross-sectional profile of the bead

Fig. 7. Schematic diagram of the combined model consisting of the ANN and the geometric model

Fig. 8. Results of the ANN model compared with the experimental measurements

Fig. 9. Comparison between geometric model output (W, H) and experimental values in different interlayer temperatures

Fig. 10. Results of the combined model compared with the experimental measurements

Fig. 11. The derivative of the width and height with respect to the contact angle when WFS=10 m/min, TS=6 mm/s

Fig. 12. Measurement results of the cross-sectional profiles in the middle of beads deposited with WFS=7.5 m/min, TS=13 mm/s and different interlayer temperatures

Table Captions